Numerical modeling of gas hydrate recycling in complex media: Implications for gas migration through strongly anisotropic layers

A. Peiraviminaei[1], **S. Gupta**[2], **B. Wohlmuth**[1]

[1]Department of Mathematics, Technical University of Munich, Munich, Germany

[2]GEOMAR Helmholtz Center for Ocean Research Kiel, Kiel, Germany

Corresponding author: A. Peiraviminaei, peiravim@ma.tum.de

Abstract

Burial driven recycling is an important process in the natural gas hydrate (GH) systems worldwide, characterized by complex multiphysics interactions like gas migration through an evolving gas hydrate stability zone (GHSZ), competing gas-water-hydrate (i.e. fluid-fluid-solid) phase transitions, locally appearing and disappearing phases, and evolving sediment properties (e.g., permeability, reaction surface area, and capillary entry pressure). Such a recycling process is typically studied in homogeneous or layered sediments. However, there is mounting evidence that structural heterogeneity and anisotropy linked to normal and inclined fault systems or anomalous sediment layers have a strong impact on the GH dynamics. Here, we consider the impacts of such a structurally complex media on the recycling process. To capture the properties of the anomalous layers accurately, we introduce a fully mass conservative, high-order, discontinuous Galerkin (DG) finite element based numerical scheme. Moreover, to handle the rapidly switching thermodynamic phase states robustly, we cast the problem of phase transitions as a set of variational inequalities, and combine our DG discretization scheme with a semi-smooth Newton solver. Here, we present our new simulator, and demonstrate using synthetic geological scenarios, a) how the presence of an anomalous high-permeability layer, like a fracture or brecciated sediment, can alter the recycling process through flow-localization, and more importantly, b) how an incorrect or incomplete approximation of the properties of such a layer can lead to large errors in the overall prediction of the recycling process.

1 Introduction

Methane hydrates are one of the most complex natural geosystems whose formation and dynamics is characterized by a wide range of strongly coupled and competing multi-physics processes such as gas migration through an evolving GHSZ, rapidly changing pressure-temperature-salinity fields, gas-water-hydrate (i.e., fluid-fluid-solid) phase transitions, locally appearing and disappearing phases, and evolving sediment properties (like permeability, capillary pressure, effective flow pathways, reaction surface area, etc.). Methane hydrates form an organic carbon repository in the earth, and have a significant contribution to the global carbon cycle. Besides, methane is an important greenhouse gas with drastic implications for climate (Wuebbles et al., 2017; Fuente et al., 2022), such as global warming, ocean acidification and de-oxygenation (Biastoch et al., 2011; Dickens, 2003). It has been estimated that the amount of carbon trapped in gas hydrates is more than twice the amount available in all other fossil fuels combined (Piñero et al., 2013; Burwicz et al., 2011; Archer et al., 2009), which has led to an increasing inter-

est in gas hydrates as a potential energy resource (Collett et al., 2009; Boswell & Collett, 2011). Due to massive over-pressure generation, salt water freshening, and/or changes in sediment mechanical characteristics upon destabilization, gas hydrates have also been linked to local and regional slope failures (Grozic, 2010; Geissler et al., 2015) and other subsurface features like pockmarks and pingos (Ostanin et al., 2013; Riboulot, 2018; Serié et al., 2012; Waage et al., 2019), pipes and chimneys (Yoo et al., 2013; Kang et al., 2015; Paganoni et al., 2018; Crutchley et al., 2021), and salt domes and diapirism (Lewis & Sager, 2012), among others. It is, therefore, abundantly clear that gas hydrates play a crucial role in the solid Earth system.

A key question in nearly any study of the dynamics and impacts of gas hydrates is that of its *distribution*: How does it form, where does it form, how did it evolve over gelogical time scales, and how much does it exist today. Microbial biodegradation of sedimentary organic matter in the deep biosphere generates biogenic methane gas. This generated methane migrates upward towards the sea-floor as a free gas or by advection of the porewater. Methane hydrates form where sufficient methane reaches the GHSZ where pressure, temperature, and salinity allow the formation of hydrate (You et al., 2019; Schmidt et al., 2022) e.g., in the permafrost regions and the marine sediments in the oceans and deep lakes. However the continuous sedimentation over geological time scales pushes this layer below the stability zone where methane gas is released and flows back to the new GHSZ. This process of burial-driven recycling of gas hydrates is believed to generate a high methane hydrate saturation which is economically interesting for gas production e.g., in the Gulf of Mexico with saturation of up to 90% (Flemings et al., 2020). Although the upward flow of methane gas into the GHSZ is, in general, blocked, as hydrates fill pore volumes and fractures (Nimblett & Ruppel, 2003; Burwicz et al., 2017), methane can still escape from hydrate layers within the GHSZ and reach the sea-floor (Liu & Flemings, 2006) which has huge environmental impacts. Infact, Schmidt et al (Schmidt et al., 2022) have shown that the gas hydrate (GH) layers act as a mechanical nozzle in the path of upward migrating gas where, given sufficient free gas below the hydrate layer, the gas hydrate peak acts as the throat of the nozzle and divides the gas hydrate layer into a converging part (below the throat) where gas experiences deceleration, and a diverging part (above the throat) where gas experiences acceleration. This GH-nozzle introduces an interesting dynamics that leads to a *cyclic* rebuilding of the gas hydrate layers under continuous burial.

Given the vast complexity of the gas hydrate systems, the modeling of gas hydrate dynamics in general, and burial-driven recycling in particular, poses multiple conceptual and computational challenges. One interesting challenge that is central to gas hydrate dynamics is that

of gas-water-hydrate phase transitions. In such situations methane can dissolve into and exsolve from porewater leading to a locally appearing and disappearing free-gas phase, and the gas hydrates can melt or precipitate, leading to an appearing, disappearing, and evolving solid phase. These fluid-fluid and fluid-solid interactions occur at different time scales, e.g., methane dissolution-exsolution is a fast process governed by vapor-liquid equilibrium on the geological time scales, while gas hydrate phase change is a slower process where the equilibrium assumption may not hold under rapid sedimentation, and is therefore, modeled as a kinetically-controlled process (Gupta et al., 2020). These phase transitions are in permanent competition that drives the aforementioned *cyclic* rebuilding of gas hydrates.

The numerical challenges related to the phase transitions are discussed in (Class et al., 2006; Marchand et al., 2013). Different numerical techniques have been constructed to overcome the phase transitions in multi-phase multi-components porous media models, e.g., primary variable switching (PVS) (Wu & Forsyth, 2001; Class et al., 2002), negative saturations (Panfilov & Panfilova, 2014), method of persistent variables (Neumann et al., 2013; Huang et al., 2015) and non-linear complementary problem approaches (Kräutle, 2011; Lauser et al., 2011; Ben Gharbia & Jaffré, 2014). PVS schemes are implemented in many of the hydrate reservoir simulators such as TOUGH-Hydrate (Moridis et al., 2008). Gupta et al. (Gupta et al., 2020) extended the non-linear complementary constraints approach of (Lauser et al., 2011) to gas hydrate systems, and showed that under rapidly switching phase states, this approach seems to be capable of handling the gas-water-hydrate phase transitions more accurately, robustly, and efficiently compared to the more traditional PVS schemes. Furthermore, with the help of this newly developed simulator, they were able to demonstrate the mechanics of the *hydrate nozzle* and its implications for gas migration through GHSZ during continuous burial.

Conventionally, however, gas hydrate recycling has been largely studied in 1D geological settings and the underlying sediments are assumed to be either homogeneous (Schmidt et al., 2022) or with vertically stacked topography (You et al., 2019, 2021) that is representative of the different granular materials, debris, and organic matter that was deposited over different geological times in the past. However, complex fault systems, fluid escape structures, and anomalous sediment layers have been observed in the seismic profiles cross-cutting the buried layers within the GHSZ worldwide (Paganoni et al., 2018; Portnov et al., 2019; Crutchley et al., 2021; Waage et al., 2019). In fact, the formation and propagation of focused flow pathways (pipes, chimneys) and their implications on gas migration, hydrate dynamics, and slope stability remains an important open question. Numerically, handling such anomalous lay-

ers is quite challenging in terms of how the underlying heterogeneity and anisotropy is physically modeled, how the numerical scheme approximates the related fluxes and any material interfaces and/or discontinuities, and how much additional computational effort is introduced for handling the such layers. In the past, we have used the cell centered finite volume (FV) methods for numerical discretization of our gas hydrate models (Gupta et al., 2015, 2020) because of their inherent simplicity for implementation of non-linear complementary problems (NCP), local mass conservation property, monotonicity, and low computational costs due to their low order and small two-point stencils. While FV methods offer a very robust, efficient, and reliable numerical framework for simple geological media, it is notoriously difficult to extend to unstructured meshes, fully anisotropic media, and discontinuous material interfaces. Forms of finite element (FE) (Cheng et al., 2013; Fang, 2010) and finite difference (FD) (Yu et al., 2017; Holder & Angert, 1982) methods are also commonly used for methane hydrate models, but they also face challenges related to phase transitions, local mass conservation, overshoots and undershoots (which further complicate the phase change problem), mesh sizes and local mesh anisotropy, and material interfaces. The discontinuous Galerkin (DG) finite element method generalizes the FE method by omitting continuity constraints, allowing potential jumps through numerical fluxes (Cockburn et al., 2000). Moreover, DG methods are locally conservative and a consistent flux across the element interfaces can be easily constructed. Therefore, DG methods, which are generalization of both FV and FE methods, appear to be more suitable for the numerical solution of the methane hydrate model not only because it can handle complex geometries and meshes (including hanging nodes), full material anisotropies, and jumps across material interfaces in a natural manner without additional computational overheads, but also because it preserves the local mass conservation property of the FV method while at the same time provides higher order approximations like FE methods. Moreover, DG schemes offer massive parallelization capability (Bey et al., 1996), which is very important for practical applications. In this manuscript, we, therefore, present a DG-based numerical scheme for our gas hydrate model, extended with the NCP-based semi-smooth Newton solver to handle the inequality constraints related with the phase transitions. In Section 2, we present the methane hydrate model based on (Gupta et al., 2020). In Section 3, we outline our numerical algorithm based on the DG discretization scheme summarized in the Appendix A. Finally, in Section 4, we present our numerical results. Firstly, we validate the numerical scheme and its implementation by considering a 1D scenario of burial-driven recycling that was analyzed in (Gupta et al., 2020), and secondly we simulate synthetic 2D scenarios of burial-driven recycling with

different configurations of anomalous anisotropic high-permeability layers in the path of upward migrating gas. With these numerical examples, we demonstrate the numerical capabilities of our DG-scheme, and also highlight the necessity of handling such layers with precision and care.

2 Mathematical model

We consider the gas hydrate model developed by Gupta et al.,(Gupta et al., 2020). This model is based on the theory of porous media and accounts for the following multiphysics processes: a) Dynamic evolution of the GHSZ due to changes in thermodynamic pTS states, b) migration of dissolved and gaseous methane through evolving GHSZ, c) rate-based gas hydrate phase transitions, d) exsolution-dissolution of methane in pore-water, and associated appearance and disappearance of free gas phase, e) thermal effects, including the heat of hydrate phase change, f) salinity changes, including feedbacks on methane solubility as well as hydrate stability, and g) changing sediment properties due to changes in pore-voids due to hydrate phase changes. A detailed model description including underlying assumptions can be found in (Gupta et al., 2020). For completeness, a summary of the main governing and constitutive equations is presented in Table 1b-1c. We show the functional dependencies of the model parameters in Table 1d.

Table 1: Summary of Mathematical Model

Preliminaries

Let Ω be a bounded domain with Lipschitz boundary in $\mathbb{R}^d$, $d = \{1, 2\}$. $\partial\Omega_D$ and $\partial\Omega_N$ denote the Dirichlet and Neumann parts of the boundary respectively and $\mathbb{T} := [0, t_{end}]$ denotes the time interval. Subscript $\beta \in \{h, g, w\}$ denotes three pore-filling phases (gas(g), water(w) and hydrate (h)), subscript $\alpha \in \{g, w\}$ denotes two fluid phases (gas(g), water(w)) and superscript $\kappa \in \{M, H, c\}$ denotes three components (Methane(M), Water(H) and salts(c)) in a porous medium. We introduce the following functions as model variables,

$$\begin{aligned} s_\beta &: \Omega \times \mathbb{T} \longrightarrow [0,1] && \text{Saturation of phase } \beta \\ \chi_\alpha^\kappa &: \Omega \times \mathbb{T} \longrightarrow [0,1] && \text{Mole fraction of component } \kappa \text{ in phase } \alpha \\ p_\alpha &: \Omega \times \mathbb{T} \longrightarrow \mathbb{R} && \text{Pore-pressure distribution of phase } \alpha \\ T &: \Omega \times \mathbb{T} \longrightarrow \mathbb{R} && \text{Temperature} \end{aligned} \tag{1}$$

Let $\mathbf{U}$ be the vector of model primary variables, which is some subset of the above introduced functions.

(a) Summary of mathematical model, preliminaries

Governing Equations	
Mass balance for each component $\kappa = M, H, c$	$A^\kappa(\mathbf{U}) := \sum_\alpha \partial_t\big(\phi\, \rho_\alpha\, \chi_\alpha^\kappa\, s_\alpha\big) + \sum_\alpha \nabla.\big(\rho_\alpha\, \chi_\alpha^\kappa\, \mathbf{v}_\alpha\big) + \sum_\alpha \nabla.\big(\phi\, s_\alpha\, \mathbf{J}_\alpha^\kappa\big) - \dot{g}^\kappa = 0, \quad \text{in } \Omega \times \mathbb{T}$ (2)
Mass balance for hydrate-phase	$A^h(\mathbf{U}) := \partial_t\big(\phi\, \rho_h\, s_h\big) - \dot{g}^h = 0, \quad \text{in } \Omega \times \mathbb{T}$ (3)
Energy balance	$A^e(\mathbf{U}) := \partial_t\big((1-\phi)\, \rho_s\, u_s + \phi \sum_\beta \rho_\beta\, u_\beta\, s_\beta\big) - \nabla.\big(k_{eff}^{th} \nabla T\big) + \sum_\alpha \nabla.\big(\rho_\alpha\, h_\alpha\, \mathbf{v}_\alpha\big) - \dot{Q}_h = 0, \text{ in } \Omega\times\mathbb{T}$ (4)
NCP related to appearance-disappearance of free-gas phase	$A^{ncp1}(\mathbf{U}) := s_g - max\big\{0,\, s_g - 1 + \sum_\kappa \chi_g^\kappa\big\} = 0 \text{ in } \Omega\times\mathbb{T},$ (5)
NCP related to appearance-disappearance of pore-water phase	$A^{ncp2}(\mathbf{U}) := s_w - max\big\{0,\, s_w - 1 + \sum_\kappa \chi_w^\kappa\big\} = 0 \text{ in } \Omega\times\mathbb{T},$ (6)

(b) Summary of mathematical model, governing equations

Closure and constitutive relationships	
Closure relationships For each α	$\sum_{\beta} s_\beta = 1$ (7) $\sum_{\kappa} \chi_\alpha^\kappa = 1$ if $s_\alpha > 0$ or $\sum_{\kappa} \chi_\alpha^\kappa < 1$ if $s_\alpha = 0$ (8)
Phase velocities based on Darcy's law	$\mathbf{v}_\alpha = -\mathbf{K}\frac{k_{r\alpha}}{\mu_\alpha}\left(\nabla P - \rho_\alpha \mathbf{g}\right)$ (9) with $\mathbf{K} = \mathbf{K}_0\left(1-s_h\right)^{\frac{5m+4}{2m}}$, $k_{rw} = s_{we}^{\frac{2+3\lambda}{\lambda}}, \quad k_{rg} = (1-s_{we})^2\left(1-s_{we}^{\frac{2+\lambda}{\lambda}}\right)$ and $s_{we} = \frac{s_w - \sum_\alpha S_{\alpha r}}{1 - s_h - \sum_\alpha S_{\alpha r}}$
Diffusive solute flux based on Fick's law	$\mathbf{J}_\alpha^\kappa = -\tau \mathbf{D}_\alpha^\kappa \rho_\alpha \nabla \chi_\alpha^\kappa$ s.t., $\sum_\alpha \mathbf{J}_\alpha^\kappa = 0$ (10)
Capillary pressure based on Brooks-Corey model	$p_g - p_w = p_c = P_0\, s_{we}^{-1/\lambda}\left(1-s_h\right)^{-\frac{m\lambda-1}{m\lambda}}$ (11)
Hydrate phase change kinetics	$\dot{g}^M = k^r A_{rs} \mathtt{M}^M \left(p_e - p_g\right)$, $\dot{g}^H = \dot{g}^M N_h \frac{\mathtt{M}^H}{\mathtt{M}^M}$, $\dot{g}_h = -\dot{g}^M \frac{\mathtt{M}_h}{\mathtt{M}^M}$, $\dot{Q}_h = \frac{\dot{g}_h}{\mathtt{M}_h}\left(a_1 + a_2 T\right)$ (12)
Vapour-Liquid Equilibrium (VLE)	Henry's law: $z^M \chi_g^M p_g = H_w^M \chi_w^M$ (13) Raoult's law: $\chi_g^H p_g = P_{sat}^H \chi_w^H$ (14)

(c) Summary of mathematical model, closure and constitutive relationships

List of model parameters
$M^\kappa \rightarrow$ Molar masses ; $\rho_\beta\left(p_\beta, T, \chi_w^c\right) \rightarrow$ phase densities; $\mu_\alpha\left(p_\alpha, T\right) \rightarrow$ fluid dynamic viscosities; $\mathbf{D}_\alpha^\kappa\left(p_\alpha\right) \rightarrow$ Fickian diffusion coefficient of component κ in fluid phase α; $\tau\left(\mathbf{x}\right) \rightarrow$ sediment tortuosity; $\mathbf{K}_0\left(\mathbf{x}\right) \rightarrow$ absolute permeability tensor; $S_{\alpha r(\mathbf{x})} \rightarrow$ residual phase saturation; $\lambda\left(\mathbf{x}\right) \rightarrow$ material parameter related to sediment grain-size distribution; $0 < m\left(\mathbf{x}\right) \leq 3 \rightarrow$ material parameter related to sphericity of hydrate growth; $P_0\left(\mathbf{x}\right) \rightarrow$ capillary entry pressure; $k^r \rightarrow$ intrinsic reaction rate of hydrate phase change; $A_{rs}\left(\mathbf{x}, s_\beta\right) \rightarrow$ reaction surface area available for hydrate phase change; $p_e\left(T, \chi_w^c\right) \rightarrow$ hydrate equilibrium pressure; $a_1, a_2 \rightarrow$ empirical constants related to heat of hydrate phase change; $H_w^M\left(p_w, T, \chi_w^c\right) \rightarrow$ Henry's solubility coefficient for methane gas in water; $P_{sat}^H\left(p_g, T, \chi_w^c\right) \rightarrow$ saturated vapour pressure; and $z^M\left(p_g, T\right) \rightarrow$ compressibility factor for methane gas, evaluated using Peng-Robinson equation of state. We assume that $\chi_g^c = 0$, $\dot{g}^c = 0$. For brevity of presentation, we only show the functional dependencies of the model parameters. The exact functional relationships can be found in detail in (Gupta et al., 2020).

(d) Summary of mathematical model, list of model parameters

To solve the 7 governing equations (2-6), we choose from the set of all model variables (1),

$$\mathbf{U} := \left(p_w, T, s_g, s_h, \chi_w^M, \chi_g^H, \chi_w^c\right) = \left(\mathbf{U}_1, \mathbf{U}_2, ..., \mathbf{U}_7\right)$$

as the primary variables.

Let $C = \{M,\ H,\ h,\ c,\ e,\ ncp1,\ ncp2\}$ be the set of indices of the corresponding equations (2-6). We remark that the number of equations is equal to the number of primary variables and thus after discretization we obtain a quadratic system matrix. Moreover, let $\partial\Omega_i^D \subseteq \partial\Omega$ and $\partial\Omega_i^N \subseteq \partial\Omega$ be the corresponding Dirichlet and Neumann boundary conditions for $\mathbf{U}_i$.

Then, we have the following nonlinear problem,

Problem 1. *Find* $\mathbf{U} : \Omega \times \mathbb{T} \longrightarrow \mathbb{R}^7$ *such that*

$$\begin{aligned}
\mathcal{A}(\mathbf{U}) &:= [A^\iota(\mathbf{U})]_{\iota \in C} = 0 \quad \textit{in } \Omega \times \mathbb{T}, \\
\mathbf{U}(x,0) &= \mathbf{U}^0 \qquad \textit{in } \Omega, \\
\mathbf{U}_i(x,t) &= \mathbf{U}_i^D \qquad \textit{on } \partial\Omega_i^D \times \mathbb{T}, \\
\nabla \mathbf{U}_i . \vec{n}_i &= \mathbf{U}_i^N \qquad \textit{on } \partial\Omega_i^N \times \mathbb{T},
\end{aligned} \tag{15}$$

where $\mathbf{U}^0$ *,* $\mathbf{U}_i^D$ *and* $\mathbf{U}_i^N$ *are given functions.*

Note that this problem is composed of a strongly coupled and highly nonlinear system of differential algebraic system of equations with four partial differential equation (2,4), one ordinary differential equation (3), and two algebraic constraints (5-6).

3 Numerical Algorithm

Problem (1) is discretized in space using a DG method of order q defined on a quadrilateral mesh with $\mathtt{N}_h$ elements. A fully Implicit Euler (IE) method is used to discretize the ODE system resulting from the spatial DG discretization. A brief description of the discretization scheme is given in Appendix (A). The resulting nonlinear residual equations can be represented in compact form as follows, (A22),:

$$\mathcal{R}(\mathbb{U}^{n+1}, \mathbb{U}^n) = 0, \qquad \mathbb{U}^{n+1},\ \mathbb{U}^n \in \mathbb{R}^{\mathbf{N}_h}, \tag{16}$$

where $\mathbb{U}^n$ is the solution vector at time t_n.

The nonlinear system (16) is linearized using a semi-smooth Newton solver, see (Wohlmuth, 2011) and references therein, which ensures that the rapidly switching phase states due to phase

transitions remain consistent within each Newton step. Time step sizes Δt_n are adaptively adjusted according to heuristical rules based on the Newton performance, i.e., Δt_n increases by 20% if the Newton method converges in less than 5 iterations, decreases by 20% if the Newton method converges in more than 8 iterations, remains unchanged if the number of iterations of the Newton method is between 5 and 8, compared to Δt_{n-1}. If the Newton Solver does not converge within 10 iterations, then we redo the time step with a step length of $\frac{\Delta t_n}{2}$.

In the following, we outline our numerical algorithm for solving Equation (16). $\mathbb{U}^0$ is the initial solution vector, k is the Newton iteration superscript, and $\mathcal{J}(\mathbb{U}^{k,n})$ is the Jacobian matrix of the residual vector $\mathcal{R}$ at $\mathbb{U}^{k,n}$. Moreover, the algorithm contains the following numerical parameters: $\Delta t_{max}, \Delta t_{min} \rightarrow$ maximum and minimum time-steps allowed for the adaptive time-stepping; $tol \rightarrow$ maximum error accepted for the residual functional $\mathcal{R}$; $k_{max} \rightarrow$ maximum number of Newton steps considered at each time-step; $k_1, k_2 \rightarrow$ number of newton steps to adapt time-step sizes.

The numerical algorithm 0 is implemented using the software framework DUNE-PDElab (Bastian, 2010), version 2.7.0, (`https://www.dune-project.org/modules/dune-pdelab/`). To solve the linear system in line (8) of the algorithm, we use an in-built biconjugate gradient stabilized method (BiCGSTAB), (Blatt et al., 2016), as iterative solver for the linearized system. In all numerical examples presented in this manuscript, the parameters of the DG scheme and the numerical algorithm are chosen as

$$\begin{aligned} k_{max} = 10, \quad k_1 = 4, \quad k_2 = 8, \quad tol = 10^{-6}, \\ \sigma_p = \sigma_s = \sigma_x = \sigma_T = 10, \qquad \Theta = 0. \end{aligned} \tag{17}$$

Algorithm 0: Newton Method, Adaptive Time Control

Input: $\Delta t_{max} > \Delta t_0 > \Delta t_{min} > 0$, $tol > 0$, k_{max}, k_1, $k_2 \in \mathbb{N}$, $\mathbb{U}^0$

Output: $\mathbb{U}^n,\ n = 1, 2, 3, \cdots$

$n \leftarrow 0,$

While $t_{n+1} \in \mathbb{T}$ **do** {

  if $\Delta t_n < \Delta t_{min}$ **do** {

    stop ▷ *change the discretization parameters, see Appendix* (A)

  }

  $k \leftarrow 0, \quad \mathbb{U}^{k,n+1} \leftarrow \mathbb{U}^n$ ▷ *initializing Newton method*

  While $\|\mathcal{R}(\mathbb{U}^{k,n+1})\| > tol$ **do** {

    Solve $\mathcal{J}(\mathbb{U}^{k,n+1})\mathbb{E}^k = -\mathcal{R}(\mathbb{U}^{k,n+1})$ ▷ *linearization*

      $\mathbb{U}^{k+1,n+1} \leftarrow \mathbb{U}^{k,n+1} + \mathbb{E}^k$

    $k \leftarrow k + 1$

    if $k > k_{max}$ **do** {

      $\Delta t_n \leftarrow (0.5 \times \Delta t_n)$ ▷ *reducing time step size*

      restart from (3)

    }

  }

  if $k < k_1$ **do** {

    $\Delta t_{n+1} \leftarrow (1.2 \times \Delta t_n)$ ▷ *increasing time step size*

  }

  if $k_2 < k \leq k_{max}$ **do** {

    $\Delta t_{n+1} \leftarrow (0.8 \times \Delta t_n)$ ▷ *reducing time step size*

  }

  $\mathbb{U}^{n+1} \leftarrow \mathbb{U}^{k,n+1}$

  $n \leftarrow n + 1$

}

4 Numerical Results

Our main motivation for the development of this new simulation framework based on the DG method arose from the need for accurate and robust handling of the multiphysics dynamics of the MHR problems in complex geological media, especially in relation with large local anisotropy and material heterogeneities. Our existing simulation environment (Gupta et

al., 2020) is based on a finite volume based numerical scheme which offers many advantages like being fully locally mass-conservative, monotonic (i.e., no overshoots and undershoots, even with coarse mesh), conceptually simpler (in terms of implementation of active/in-active sets related with the semi-smooth Newton method), and computationally cheaper (due to low order and therefore fewer degrees of freedom). However, it has a major limitation when the subsurface properties show large local anisotropies and other complex material properties such as cross-cutting features like fractures and brecciated layers. With that in mind, we present here two numerical examples: 1) **Example 1** considers a simplified 1D MHR scenario in a fully homogeneous medium with continuous burial at a constant rate. This example is used as a *benchmark* to validate the implementation of our DG scheme against our FV simulator, and 2) **Example 2** simulates MHR scenarios in a more complex 2D setting where two different configurations of idealized anomalous anisotropic material layers are considered in the GHSZ. The goal of Example 2 is to demonstrate the capability of our simulator in handling such complex sediment structures, and to highlight the impacts on prediction accuracy that can arise from incomplete and/or inaccurate approximation of the properties of these complex sediment structures.

Example 1. *Validation scenario: MHR in a homogeneous domain*

This scenario, developed and analyzed in (Gupta et al., 2020), is based on the geological setting of a buried channel-levee (BCL) complex in the Danube paleo delta (Black Sea) that is believed to have deposited its levees between 320 and 75 kilo-annum before present (ka BP) (Zander et al., 2017). Here, we simulate how a continuous deposition of sediment layers over the past 300 ka could have affected the MHR though the gas hydrate stability zone (GHSZ). Hence, the initial setting is based on the paleo conditions existing at 300 ka BP, and the top of the computational domain is pinned at the corresponding paleo seafloor. We consider a 1D domain $\Omega = [-500, 0]$. The problem schematic is shown in Figure 1.

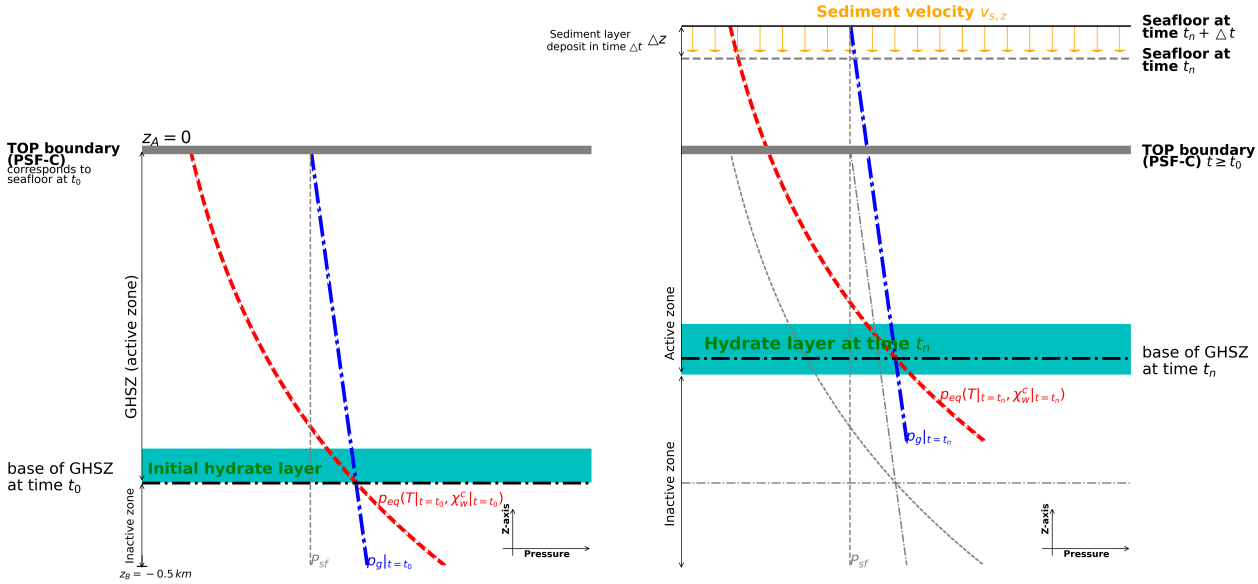

Figure 1: Problem setting for Example 1, recreated from . *left*: The initial state of the system and the corresponding hydrate layer inside the GHSZ, $t = t_0 = 0$ (i.e., 300 ka BP). *right*: The state of the system at $t = t_n > 0$, indicating how the GHSZ shifts as a result of sedimentation over time.

Initial and boundary conditions are specified in Table 2. For the prescribed paleo pTS conditions, the base of the GHSZ (bGHSZ) (i.e., depth at which $p_e = p_g$) lies at 400 m below seafloor (mbsf). At $t = 300$ ka BP, we assume that there is no free gas anywhere in the domain, and methane hydrate is located in the interval $[320\ , 400]$ mbsf, directly above the bGHSZ. Furthermore, we assume that the deposition of the sediment layer at $z = 0$ (i.e., paleo seafloor) occurs with constant sedimentation rate $v_{s,z} = 1\,mm/year$ over a period of 300 ka (i.e. from 300 ka BP to present day).

Initial conditions $t = 0$	
$\Omega = [-500, 0]$	$p_w = 15\,MPa + \rho_w \mathbf{g}(z_{sf} - z)$ $T = 4^\circ\,C + d_z T_G(z_{sf} - z)$ $s_g = 0$ $\chi_w^c = 0.0096$ $\chi_w^M = 0$ $\chi_g^H = \chi_{g,sat}^H(p_g, T)$
$-400\,m \leq z \leq -320\,m$ $-400\,m \geq z \; or \; z \geq -320\,m$	$s_h = 1.2(\frac{z+320}{-400+320})(\frac{z+400}{-320+400})$ $s_h = 0$
Boundary conditions $x \in \partial\Omega, \;\; t > 0$	
$z = z_{sf}$	$p_w = 15\,MPa + \rho_w \mathbf{g} v_{s,z}(t_n + \Delta t)$ $T = 4^\circ\,C + d_z T_G v_{s,z}(t_n + \Delta t)$ $s_g = 0$ $\chi_w^c = \chi_w^c\|_{t=0}$
$z = -500$	$\mathbf{v}_w = 0$ $\mathbf{v}_g = 0$ $\nabla \chi_w^c = 0$ $\partial_z T = d_z T_G$

Table 2: Initial and boundary conditions for Example 1, $d_z T_G = 35^\circ\,C/km$, $v_{s,z} = 1\,mm/year$

As sedimentation occurs, more and more sediment layers accumulate above the paleo seafloor, leading to an increasing pressure and temperature at the paleo seafloor boundary. These changes cause the bGHSZ to shift upwards and destabilize the overlying gas hydrate layer. As gas hydrates melt, methane is released, which in sufficiently high quantity can lead to a free-gas phase to form and accumulate at the base of the gas hydrate layer. Schmidt et al., 2022, (Schmidt et al., 2022), have shown that gas migration through the GHSZ in this scenario is highly dynamic and occurs in cycles. The gas hydrate layer acts as a converging-diverging nozzle in the path of upward migrating free gas.

In Figure 2, snapshots of methane hydrate dissociation $\rightarrow$ gas migration $\rightarrow$ hydrate reformation is shown from 300 ka BP to present day. To be consistent with the mathematical model, Problem 1, we consider sedimentation time period of 300 ka from $t = 0$ to $t = 300\;Kyr$ where $t = 0$ corresponds to the 300 ka BP.

The process of gas migration through GHSZ and MHR can be summarized as follows: Free gas phase appears below the melting gas hydrate layer and flows upwards due to buoyancy. However, as the gas flows through the hydrate layer, the gas velocity continuously decreases because of decreasing permeability due to increasing hydrate saturation (converging

part of the hydrate nozzle). Once the gas phase passes the point with maximum hydrate saturation s_h (throat of the hydrate nozzle), the gas velocity starts to increase (diverging part of the hydrate nozzle). As gas escapes the hydrate layer into the overlying GHSZ, reformation of methane hydrate starts. The new hydrate layer continuously grows consuming the free gas provided by the dissociation of the previous methane hydrate layer, as shown in Figure 2.

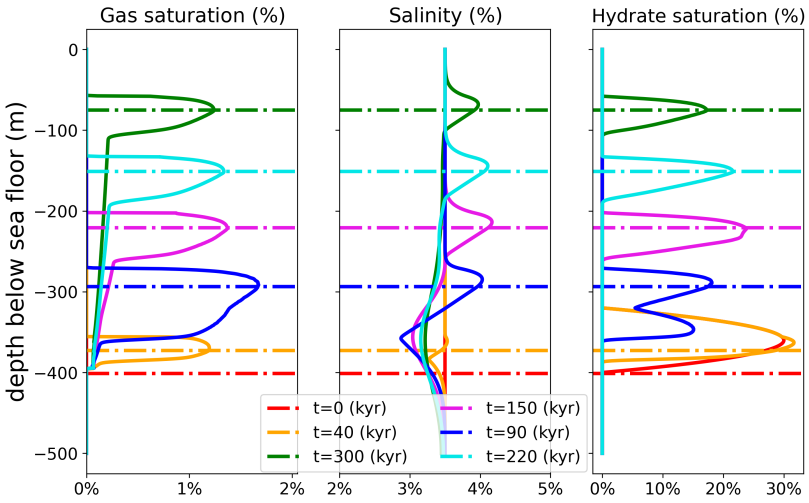

Figure 2: MHR process from $t = 0$ to 300 Kyr for Example 1. The horizontal dashed lines show the base of GHSZ. $q = 2$, $h = 0.5(m)$

While the increase of temperature by the geothermal gradient has a global effect on the equilibrium pressure, salinity has a local effect on the equilibrium pressure. This is due to the fact that heat diffuses much faster than salt (see Figure 3).

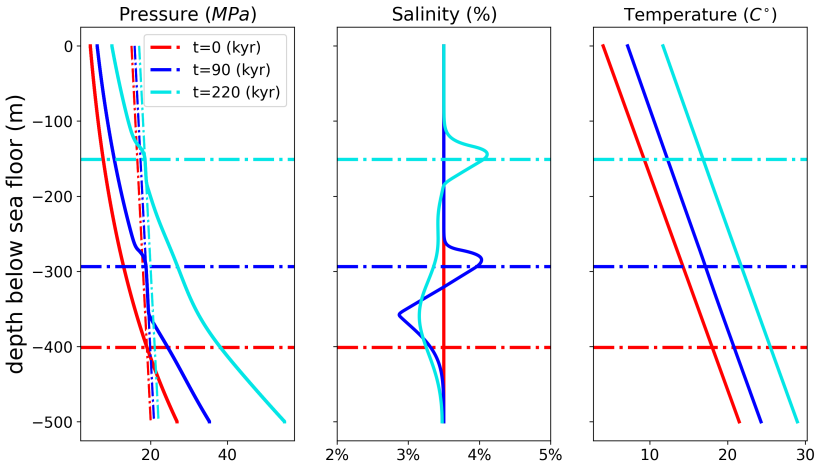

Figure 3: Upward shifting of GHSZ of Example 1. *left:* Gas pressure (dashed), Equilibrium pressure (solid); *middle:* Salinity; *right:* Temperature. The horizontal dashed lines show the base of GHSZ. $q = 2,\ h = 0.5(m)$.

Figure 4 shows linear to fourth order approximation of the solution of Example 1. The reference solution obtained on a fine mesh, $h = 0.25$ (m), and order $q = 4$ is plotted with the dashed line. To reduce the spurious oscillations, we implemented a linear polynomial reconstruction for the gas saturation based on the weighted mean derivatives of the solution in the neighboring elements (Frerichs & John, 2021). In Figure 5, snapshots of gas saturation are plotted for $h = 0.5$ and $q = 1$ at $t = 100$ Kyr with and without slope limiter. We chose $t = 100$ Kyr, because as it is shown in Figure 2, the maximum gas saturation occurs around $t = 100$ Kyr and the escaping of gas from hydrate layer leads to oscillatory sharp front. It shows that sharp gradients of gas saturation are avoided by implementing the slope limiter.

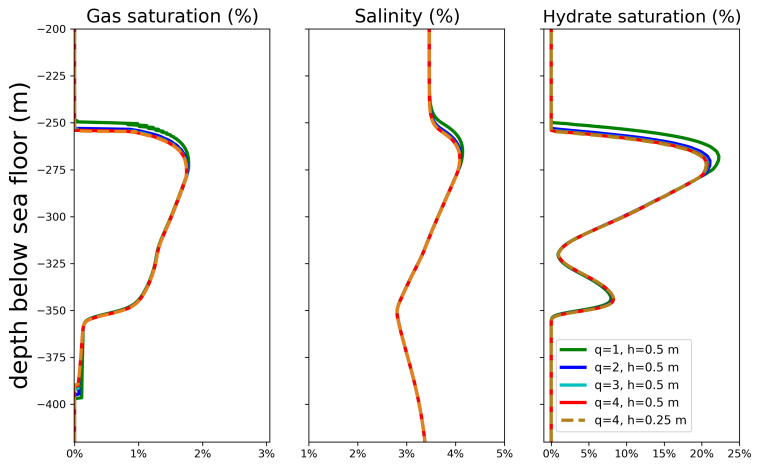

Figure 4: Linear to forth order approximation of the solution of Example 1, $t = 100$ (Kyr).

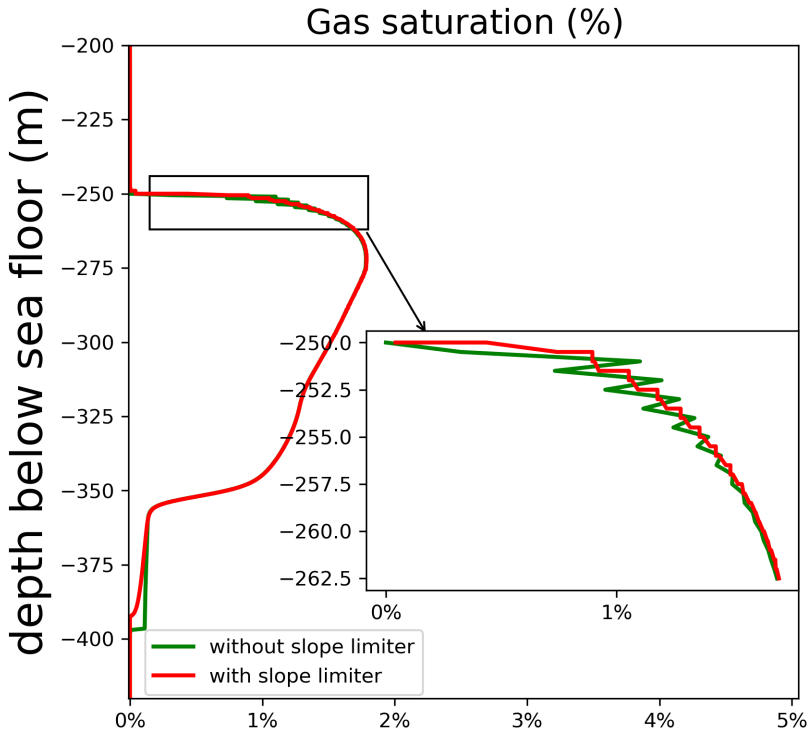

Figure 5: Slope limiter, from , implemented for gas saturation for the solution of Example 1, $t = 100$ (Kyr), $q = 1$, $h = 0.5(m)$.

In Figure 6, the convergence behavior of the nonlinear solver for a mesh with $h = 0.125(m)$ is shown. Time step sizes drop when gas phase appears. However, they mostly remain bigger than 10 years, while in (Gupta et al., 2020) Figure $4.b$, Gupta et al., compared the time step size of NCP and PVS approaches which showed that even for the bigger mesh size $h = 0.3125(m)$ the maximum time step size of 10 years was scarcely achieved.

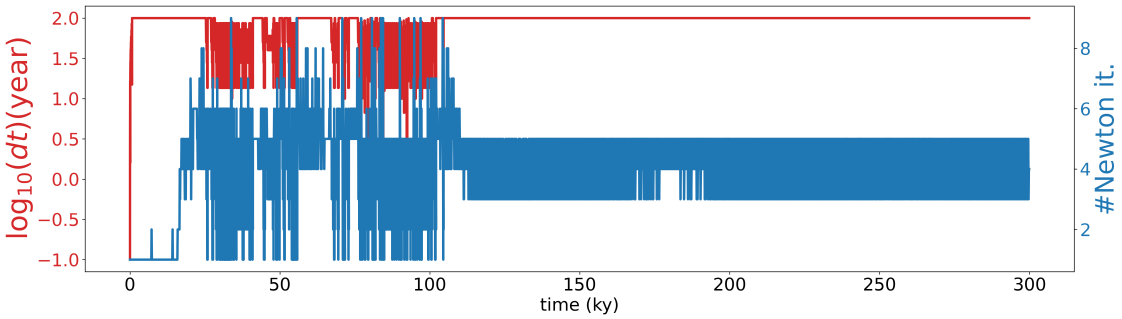

Figure 6: Numerical results for Example 1, the evolution of the time-step size during the simulation, $q = 1$, $h = 0.125(m)$. Time step sizes drop when gas phase appears, however, they mostly remain bigger than 10 years,

Example 2. *2D scenario: Gas flow through GHSZ with heterogeneous material property*

Here, we extend the above 1D scenario by introducing an anomalous material layer with high-permeability and large anisotropy within the paleo GHSZ. The problem schematic is shown in Figure 7, and the initial and boundary conditions are similar to Example 1 and for completeness are given in Table 3. Two different configurations are considered for the permeability tensors of the anomalous material layer, as shown in Figure 7, where $\mathbf{K}_2$ is a rotation of a by K_F scaled $\mathbf{K}_1$ and θ is the rotation degree of $\mathbf{K}_1$.

$$\mathbf{K}_1 = \begin{bmatrix} K_0 & 0 \\ 0 & K_0 \end{bmatrix}, \quad \mathbf{K}_2 = \begin{bmatrix} \cos(\theta) & -\sin(\theta) \\ \sin(\theta) & \cos(\theta) \end{bmatrix} \begin{bmatrix} K_F K_0 & 0 \\ 0 & K_F K_0 \end{bmatrix}, \tag{18}$$

K_0 is the absolute scalar permeability of the background sediment and K_F is a scaling factor for the absolute permeability of the anomalous layer.

Initial conditions $t = 0$	
$\Omega = [0, 400] \times [-500, 0]$	$p_w = 15\,MPa + \rho_w \mathbf{g}(z_{sf} - z)$ $T = 2.2^\circ\,C + d_z T_G (z_{sf} - z)$ $s_g = 0$ $\chi_w^c = 0.0096$ $\chi_w^M = 0$ $\chi_g^H = \chi_{g,sat}^H(p_g, T)$
$-460\,m \leq z \leq -380\,m$ $-460\,m \geq z \; or \; z \geq -380\,m$	$s_h = 1.2(\frac{z+380}{-460+320})(\frac{z+460}{-380+460})$ $s_h = 0$
Boundary conditions $x \in \partial\Omega,\ t > 0$	
$z = z_{sf}$	$p_w = 15\,MPa + \rho_w \mathbf{g} v_{s,z}(t_n + \Delta t)$ $T = 2.2^\circ\,C + d_z T_G v_{s,z}(t_n + \Delta t)$ $s_g = 0$ $\chi_w^c = \chi_w^c\|_{t=0}$
$x = 0 \; or \; x = 400 \; or \; z = -500$	$\mathbf{v}_w = 0$ $\mathbf{v}_g = 0$ $\nabla\chi_w^c = 0$
$z = -500$	$\partial_z T = d_z T_G$

Table 3: Initial and boundary conditions for both configurations case-1 and case-2 of Example 2, with regional thermal gradient $d_z T_G = 35^\circ\,C/km$ and burial velocity $v_{s,z} = 1\,mm/year$.

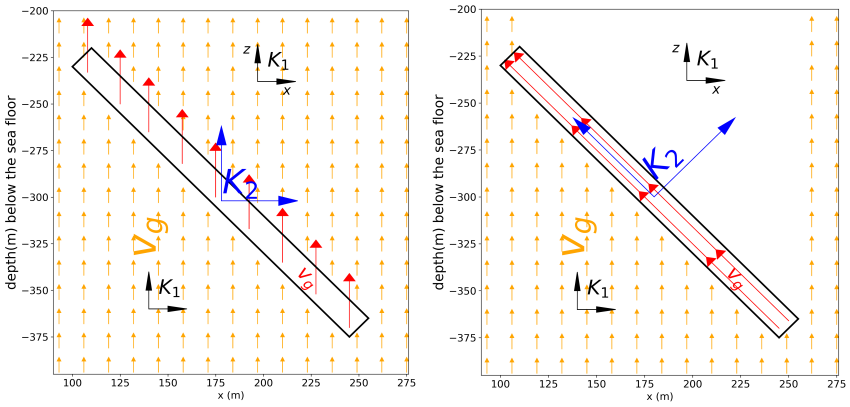

(a) Heterogeneous domain, $\theta = 0^\circ$ (b) Heterogeneous domain, $\theta = 45^\circ$

Figure 7: Schematic setting of Example 2 showing the anomalous anisotropic layer where v_g is the gas velocity, K_1 and K_2 are permeability tensors.

In the first configuration, the degree of rotation is $0°$. This is the simplest form of anisotropy, and the only form that can be handled by our finite volume based numerical solver with linear two-point flux approximations. This form, however, ignores the strongly directional properties of such a layer (e.g., flow through fractures). The second configuration accounts for this by rotating the permeability tensor along the layer axis. Such form of anisotropy (with full tensor) cannot be handled with a linear two-point flux approximation in a finite volume scheme, and instead, requires advanced methods like multi-point flux approximations or non-linear two-point flux approximations, both of which are computationally more expensive and conceptually more complicated. However, in DG discretization, any form of material anisotropy can be handled easily without additional overheads. The direction of the gas velocity depends on the permeability tensor of the layers, as schematically shown in Figure 7. When gas reaches the high permeable layer in case of the rotated permeability tensor, it will flow dominantly along the layer, bypassing the regions above the layer, as shown in Figure 7b.

Figure 8 shows snapshots of the MHR and gas migration processes for configuration with $\theta = 0°$, and Figure 9 shows snapshots for the configuration with $\theta = 45°$. Notice how in the former, *more* gas is transported to the region above the anomalous layer and a thicker hydrate layer with higher saturation develops, while in the latter, gas is completely diverted through the anomalous layer, and the gas migration through the GHSZ is fully localized within a focused flow channel that looks strikingly similar to the chimney-like fluid escape structures observed in seimic profiles, see (Crutchley et al., 2021; Waage et al., 2019). Notice also that the gas ascent towards the seafloor is much faster in the latter configuration compared to the former. What is especially interesting is that even though the anomalous layer has the same geometry and same heterogeneity in both configurations, the gas migration shows completely different behaviour due to the nature of the anisotropy. These idealized scenarios clearly demonstrate how the approximation of the properties of the complex sediment structures can lead to remarkably large deviations in the system dynamics.

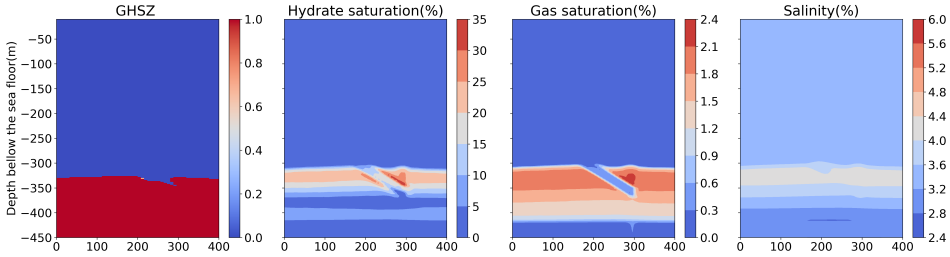

(a) $t = 65$ Kyr (235 ka BP)

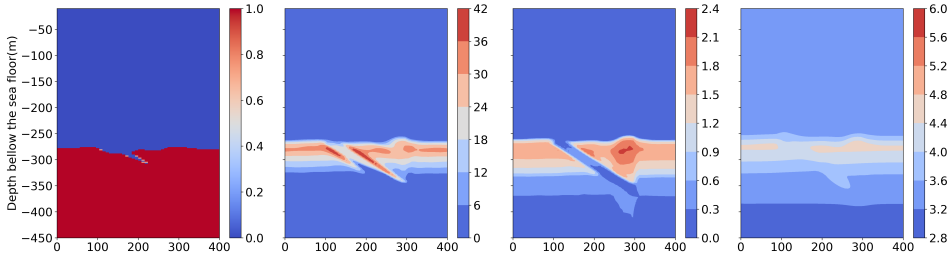

(b) $t = 90$ Kyr (210 ka BP)

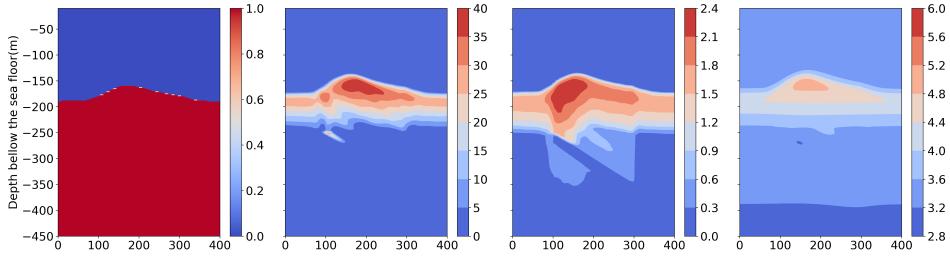

(c) $t = 150$ Kyr (150 ka BP)

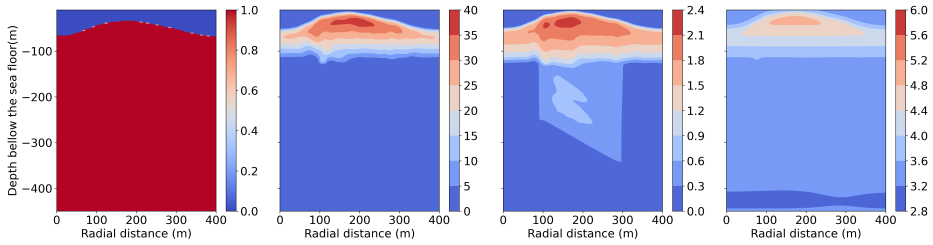

(d) $t = 230$ Kyr (70 ka BP)

Figure 8: Numerical results for case-1 of Example 2. The figure shows snapshots of (from left to right): $GHSZ$, s_h, s_g, χ_w^c within the domain of interest $\Omega = [0, 400] \times [-500, 0]$ at different times. Note, for GHSZ, a value of 1 indicates an unstable zone, and 0 indicates a stable zone.

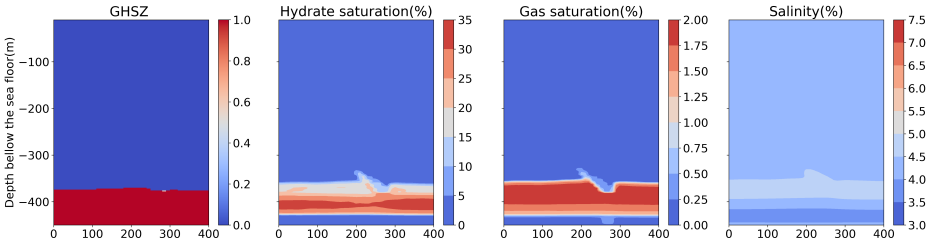

(a) $t = 65$ Kyr (235 ka BP)

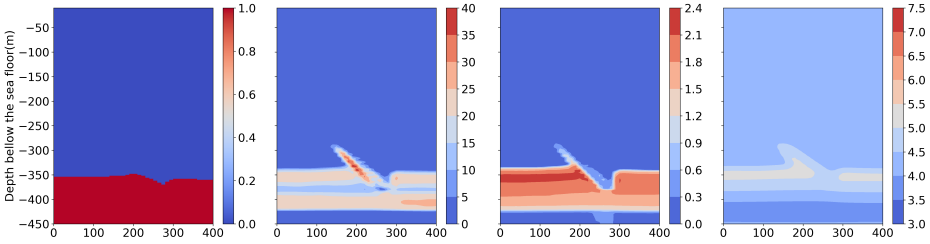

(b) $t = 75$ Kyr (225 ka BP)

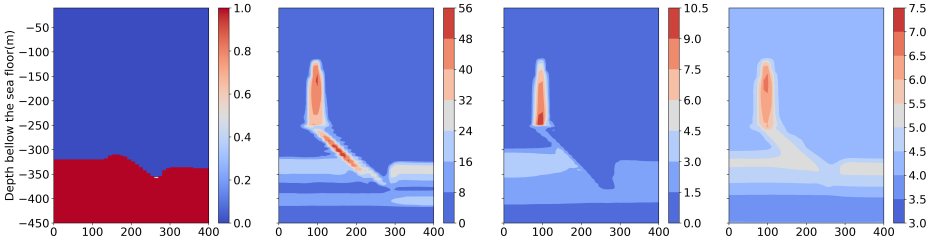

(c) $t = 85$ Kyr (215 ka BP)

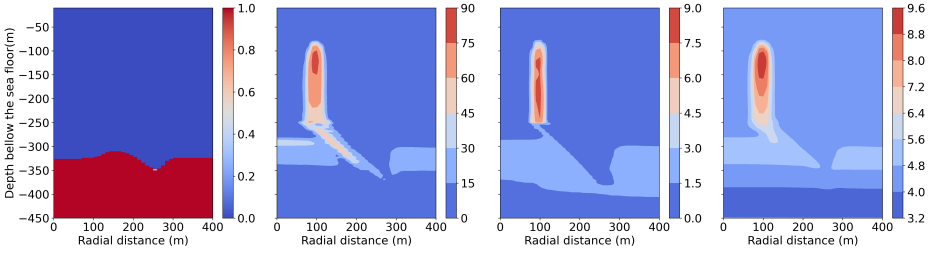

(d) $t = 90$ Kyr (210 ka BP)

Figure 9: Numerical results for case-2 of Example 2 with one heterogeneous layer. The figure shows snapshots of (from left to right): $GHSZ,\ s_h,\ s_g,\ \chi_w^c$ within the domain of interest $\Omega = [0, 400] \times [-500, 0]$ at different times. Note, for GHSZ, a value of 1 indicates unstable zone, and 0 indicates stable zone. Strong anisotropy leads to development of focused gas flow.

In fact, the development of focused gas flow in Figure 9c is a particularly interesting result with direct implications for real world scenarios. For example, seismic data of the gas hydrate system in New Zealand's southern Hikurangi subduction margin shows a network of normal faults lying within the GHSZ (Crutchley et al., 2021). Data shows a broad zone of both negative- and positive-polarity reflections (interpreted as sediment layer with coexisting free gas and gas hydrate). This zone lies directly beneath sub-vertical gas-flow conduits (possibly a combination of gas-charged normal fault and gas pipe/chimney), and extends up to the base of the regional GHSZ. In their analysis of this data, Crutchley et al. (2021) highlight the importance of considering the structural heterogeneity within GHSZ and in particular, the impact of normal faults on the gas migration through the GHSZ. Similarly, high resolution 3D seismic data from the Storfjordrenna gas hydrate pingos field in northwestern Barents Sea shows that the pingos lie on top of gas chimneys that are connected to inclined faults within the underlying free gas and hydrate?bearing sedimentary rocks (Waage et al., 2019), highlighting once again the relationship between gas hydrate dynamics and regional fault system. Our numerical scheme capture this dynamics quite well and results illustrate the role of structural heterogeneity on dynamics of gas hydrates and gas migration through GHSZ. Moreover, our results emphasize the dramatic deviations that can appear in simulated system behavior if the structural heterogeneities are not appropriately handled.

5 Conclusion

Natural gas hydrate systems are characterized by strongly coupled and highly dynamic multiphysics interactions that require sophisticated numerical schemes to capture the system behavior accurately and robustly. A particular challenge is related to the complex structure of the geological subsurface. Classically, problems like burial driven recycling are studied in homogeneous sediments, or sediments with a layered stratigraphy that follows the paleo and present seafloor topographies. Existence of strongly anisotropic anomalous layers with large contrasts in properties within the gas hydrate stability zone can lead to significant deviations in the system dynamics. An accurate prediction of these deviations is critical for estimating the present day geological carbon repositories, response of hydrate-bearing sediments to changing environmental and climate stressors, and their geomechanical stability in response to natural and anthropogenic activities. In this manuscript, we present a new numerical scheme based on the DG method for our methane hydrate model (Gupta et al., 2020). The motivation for the development of this new numerical scheme was to enhance the flexibility compared to FV ap-

proaches so that we can handle the structural complexities of the sediments more accurately, and therefore, be able to consider more realistic geological settings. The choice of the DG scheme was specifically inspired by the fact that it is locally mass conservative (like the finite volume method on which our earlier simulators are based), and can approximate the fluxes in anisotropic fields more generally without additional overheads (like larger stencils that are needed for extending finite volume schemes with methods like multi-point and nonlinear two-point flux approximations in order to capture material anisotropy). Here we show that a) the semi-smooth Newton solver for handling gas-water phase transitions performs well with a DG based discretization, b) the presented DG scheme is able to capture the multiphysics dynamics of the methane hydrate systems accurately, and c) the presented DG scheme is able to accurately capture the gas migration and hydrate recycling processes through strongly anisotropic materials. We also demonstrate that layer properties influence sensitively the numerical simulation results and incomplete knowledge can result in very large prediction errors of the recycling process.

Acknowledgments

References

Archer, D., Buffett, B., & Brovkin, V. (2009). Ocean methane hydrates as a slow tipping point in the global carbon cycle. *Proceedings of the National Academy of Sciences*, *106*(49), 20596-20601. Retrieved from `https://www.pnas.org/doi/abs/10.1073/pnas.0800885105` doi: 10.1073/pnas.0800885105

Bastian, H. F. M. S., Peter. (2010). Generic implementation of finite element methods in the distributed and unified numerics environment (dune). *Kybernetika*, *46*(2), 294-315. Retrieved from `http://eudml.org/doc/197255`

Ben Gharbia, I., & Jaffré, J. (2014). Gas phase appearance and disappearance as a problem with complementarity constraints. *Mathematics and Computers in Simulation*, *99*, 28-36. Retrieved from `https://www.sciencedirect.com/science/article/pii/S0378475413001924` (MAMERN IV–2011: The 4th International Conference on Approximation Methods and Numerical Modeling in Environment and Natural Resources- PART I) doi: https://doi.org/10.1016/j.matcom.2013.04.021

Bey, K. S., Tinsley Oden, J., & Patra, A. (1996). A parallel hp-adaptive discontinuous galerkin method for hyperbolic conservation laws. *Applied Numerical Mathemat-*

ics, *20*(4), 321-336. Retrieved from https://www.sciencedirect.com/science/article/pii/0168927495001018 (Adaptive mesh refinement methods for CFD applications) doi: https://doi.org/10.1016/0168-9274(95)00101-8

Biastoch, A., Treude, T., Rüpke, L. H., Riebesell, U., Roth, C., Burwicz, E. B., ... Wallmann, K. (2011). Rising arctic ocean temperatures cause gas hydrate destabilization and ocean acidification. *Geophysical Research Letters*, *38*(8). Retrieved from https://agupubs.onlinelibrary.wiley.com/doi/abs/10.1029/2011GL047222 doi: https://doi.org/10.1029/2011GL047222

Blatt, M., Burchardt, A., Dedner, A., Engwer, C., Fahlke, J., Flemisch, B., ... Sander, O. (2016). The Distributed and Unified Numerics Environment, Version 2.4. *Archive of Numerical Software*, *4*(100), 13–29. Retrieved from http://dx.doi.org/10.11588/ans.2016.100.26526 doi: 10.11588/ans.2016.100.26526

Boswell, R., & Collett, T. S. (2011). Current perspectives on gas hydrate resources. *Energy Environ. Sci.*, *4*, 1206-1215. Retrieved from http://dx.doi.org/10.1039/C0EE00203H doi: 10.1039/C0EE00203H

Burwicz, E., Reichel, T., Wallmann, K., Rottke, W., Haeckel, M., & Hensen, C. (2017). 3-d basin-scale reconstruction of natural gas hydrate system of the green canyon, gulf of mexico. *Geochemistry, Geophysics, Geosystems*, *18*(5), 1959-1985. Retrieved from https://agupubs.onlinelibrary.wiley.com/doi/abs/10.1002/2017GC006876 doi: https://doi.org/10.1002/2017GC006876

Burwicz, E., Rüpke, L., & Wallmann, K. (2011). Estimation of the global amount of submarine gas hydrates formed via microbial methane formation based on numerical reaction-transport modeling and a novel parameterization of holocene sedimentation. *Geochimica et Cosmochimica Acta*, *75*(16), 4562-4576. Retrieved from https://www.sciencedirect.com/science/article/pii/S0016703711002973 doi: https://doi.org/10.1016/j.gca.2011.05.029

Cheng, Y., Li, L., Yuan, Z., Wu, L., & Mahmood, S. (2013). Finite element simulation for fluid-solid coupling effect on depressurization-induced gas production from gas hydrate reservoirs. *Journal of Natural Gas Science and Engineering*, *10*, 1-7. Retrieved from https://www.sciencedirect.com/science/article/pii/S1875510012001023 doi: https://doi.org/10.1016/j.jngse.2012.10.001

Class, H., Helmig, R., & Bastian, P. (2002). Numerical simulation of non-isothermal multiphase multicomponent processes in porous media.: 1. an efficient solution tech-

nique. *Advances in Water Resources*, *25*(5), 533-550. Retrieved from https://www.sciencedirect.com/science/article/pii/S0309170802000143 doi: https://doi.org/10.1016/S0309-1708(02)00014-3

Class, H., Helmig, R., Niessner, J., & Ölmann, U. (2006). Multiphase processes in porous media. In R. Helmig, A. Mielke, & B. I. Wohlmuth (Eds.), *Multifield problems in solid and fluid mechanics* (pp. 45–82). Berlin, Heidelberg: Springer Berlin Heidelberg. Retrieved from https://doi.org/10.1007/978-3-540-34961-7_2 doi: 10.1007/978-3-540-34961-7_2

Cockburn, B., Karniadakis, G. E., & Shu, C. (2000). *Discontinuous galerkin methods* (Vol. 11). Springer Berlin, Heidelberg. Retrieved from https://doi.org/10.1007/978-3-642-59721-3 doi: 10.1007/978-3-642-59721-3

Collett, T., Johnson, A., Knapp, C., & Boswell, R. (2009). *Natural Gas Hydrates-Energy Resource Potential and Associated Geologic Hazards*. American Association of Petroleum Geologists. Retrieved from https://doi.org/10.1306/M891320 doi: 10.1306/M891320

Crutchley, G. J., Mountjoy, J. J., Hillman, J. I. T., Turco, F., Watson, S., Flemings, P. B., ... Bialas, J. (2021). Upward-doming zones of gas hydrate and free gas at the bases of gas chimneys, new zealand's hikurangi margin. *Journal of Geophysical Research: Solid Earth*, *126*(9), e2020JB021489. Retrieved from https://agupubs.onlinelibrary.wiley.com/doi/abs/10.1029/2020JB021489 (e2020JB021489 2020JB021489) doi: https://doi.org/10.1029/2020JB021489

Dickens, G. R. (2003). Rethinking the global carbon cycle with a large, dynamic and microbially mediated gas hydrate capacitor. *Earth and Planetary Science Letters*, *213*(3), 169-183. Retrieved from https://www.sciencedirect.com/science/article/pii/S0012821X0300325X doi: https://doi.org/10.1016/S0012-821X(03)00325-X

Fang, H.-L. (2010). A fully coupled thermo-hydro-mechanical model for methane hydrate reservoir simulations. In Y. Chen, L. Zhan, & X. Tang (Eds.), *Advances in environmental geotechnics* (pp. 455–461). Berlin, Heidelberg: Springer Berlin Heidelberg.

Flemings, P., Phillips, S., Boswell, R., Collett, T., Cook, A., Dong, T., ... You, K. (2020). Pressure coring a gulf of mexico deep-water turbidite gas hydrate reservoir: Initial results from the university of texas–gulf of mexico 2-1 (ut-gom2-1) hydrate

pressure coring expedition. *AAPG Bulletin*, *104*(9), 1847-1876. Retrieved from https://doi.org/10.1306/05212019052 doi: 10.1306/05212019052

Frerichs, D., & John, V. (2021). On reducing spurious oscillations in discontinuous galerkin (dg) methods for steady-state convection-diffusion equations. *Journal of Computational and Applied Mathematics*, *393*, 113487. Retrieved from https://www.sciencedirect.com/science/article/pii/S0377042721001060 doi: https://doi.org/10.1016/j.cam.2021.113487

Fuente, M. D. L., Arndt, S., Marín-Moreno, H., & Minshull, T. A. (2022, may). Assessing the benthic response to climate-driven methane hydrate destabilisation: State of the art and future modelling perspectives. *Energies*, *15*(9), 3307. Retrieved from https://doi.org/10.3390/en15093307 doi: 10.3390/en15093307

Geissler, W., Gebhardt, C., Gross, F., Wollenburg, J., Jensen, L., Schmidt-Aursch, M., & Krastel, S. (2015). Slope stability, gas hydrates, and methane seepage at the shelf north of svalbard. In *3p arctic: Polar petroleum potential conference & exhibition.* American Association of Petroleum Geologists (AAPG).

Grozic, J. L. H. (2010). Interplay between gas hydrates and submarine slope failure. In D. C. Mosher et al. (Eds.), *Submarine mass movements and their consequences* (pp. 11–30). Dordrecht: Springer Netherlands. Retrieved from https://doi.org/10.1007/978-90-481-3071-9_2 doi: 10.1007/978-90-481-3071-9_2

Gupta, S., Helmig, R., & Wohlmuth, B. (2015, Oct 01). Non-isothermal, multi-phase, multi-component flows through deformable methane hydrate reservoirs. *Computational Geosciences*, *19*(5), 1063-1088. Retrieved from https://doi.org/10.1007/s10596-015-9520-9 doi: 10.1007/s10596-015-9520-9

Gupta, S., Wohlmuth, B., & Haeckel, M. (2020). An all-at-once newton strategy for marine methane hydrate reservoir models. *Energies*, *13*(2). Retrieved from https://www.mdpi.com/1996-1073/13/2/503 doi: 10.3390/en13020503

Holder, G. D., & Angert, P. F. (1982, 09). Simulation of Gas Production From a Reservoir Containing Both Gas Hydrates and Free Natural Gas. In (Vol. All Days). Retrieved from https://doi.org/10.2118/11105-MS doi: 10.2118/11105-MS

Huang, Y., Kolditz, O., & Shao, H. (2015, Jul 09). Extending the persistent primary variable algorithm to simulate non-isothermal two-phase two-component flow with phase change phenomena. *Geothermal Energy*, *3*(1), 13. Retrieved from https://doi.org/10.1186/s40517-015-0030-8 doi: 10.1186/s40517-015-0030-8

Kang, N., Yoo, D.-G., Yi, B., & Park, S.-c. (2015, 09). Distribution and origin of seismic chimneys associated with gas hydrate using 2d multi-channel seismic reflection and well log data in the ulleung basin, east sea. *Quaternary International*, *392*. doi: 10.1016/j.quaint.2015.08.002

Kräutle, S. (2011). The semismooth newton method for multicomponent reactive transport with minerals. *Advances in Water Resources*, *34*(1), 137-151. Retrieved from https://www.sciencedirect.com/science/article/pii/S0309170810001934 doi: https://doi.org/10.1016/j.advwatres.2010.10.004

Lauser, A., Hager, C., Helmig, R., & Wohlmuth, B. (2011). A new approach for phase transitions in miscible multi-phase flow in porous media. *Advances in Water Resources*, *34*(8), 957-966. Retrieved from https://www.sciencedirect.com/science/article/pii/S0309170811000856 doi: https://doi.org/10.1016/j.advwatres.2011.04.021

Lewis, D., & Sager, W. (2012). Salt tectonics and its effect on sediment structure and gas hydrate occurrence in the northwestern gulf of mexico from 2d multichannel seismic data. *GCAGS Journal*(v.1).

Liu, X., & Flemings, P. B. (2006). Passing gas through the hydrate stability zone at southern hydrate ridge, offshore oregon. *Earth and Planetary Science Letters*, *241*(1), 211-226. Retrieved from https://www.sciencedirect.com/science/article/pii/S0012821X05007223 doi: https://doi.org/10.1016/j.epsl.2005.10.026

Marchand, E., Müller, T., & Knabner, P. (2013, Apr 01). Fully coupled generalized hybrid-mixed finite element approximation of two-phase two-component flow in porous media. part i: formulation and properties of the mathematical model. *Computational Geosciences*, *17*(2), 431-442. Retrieved from https://doi.org/10.1007/s10596-013-9341-7 doi: 10.1007/s10596-013-9341-7

Moridis, G., Moridis, G. J., Kowalsky, M. B., & Pruess, K. (2008). *Tough+hydrate v1.0 user's manual: A code for the simulation of system behavior in hydrate-bearing geologic media* (Tech. Rep.). United States. Retrieved from https://doi.org/10.2172/927149 (Research Org.: Lawrence Berkeley National Lab. (LBNL), Berkeley, CA (United States), Sponsor Org.: Earth Sciences Division, Report Number: LBNL-149E, Contract Number: DE-AC02-05CH11231) doi: 10.2172/927149

Neumann, R., Bastian, P., & Ippisch, O. (2013, Feb 01). Modeling and simulation of two-phase two-component flow with disappearing nonwetting phase. *Computational Geo-*

sciences, *17*(1), 139-149. Retrieved from https://doi.org/10.1007/s10596-012-9321-3 doi: 10.1007/s10596-012-9321-3

Nimblett, J., & Ruppel, C. (2003). Permeability evolution during the formation of gas hydrates in marine sediments. *Journal of Geophysical Research: Solid Earth*, *108*(B9). Retrieved from https://agupubs.onlinelibrary.wiley.com/doi/abs/10.1029/2001JB001650 doi: https://doi.org/10.1029/2001JB001650

Ostanin, I., Anka, Z., di Primio, R., & Bernal, A. (2013). Hydrocarbon plumbing systems above the snøhvit gas field: structural control and implications for thermogenic methane leakage in the hammerfest basin, sw barents sea. *Marine and Petroleum Geology*, *43*, 127–146.

Paganoni, M., Cartwright, J. A., Foschi, M., Shipp, C. R., & Van Rensbergen, P. (2018). Relationship between fluid-escape pipes and hydrate distribution in offshore sabah (nw borneo). *Marine Geology*, *395*, 82-103. Retrieved from https://www.sciencedirect.com/science/article/pii/S0025322717301706 doi: https://doi.org/10.1016/j.margeo.2017.09.010

Panfilov, M., & Panfilova, I. (2014, Aug 01). Method of negative saturations for flow with variable number of phases in porous media: extension to three-phase multi-component case. *Computational Geosciences*, *18*(3), 385-399. Retrieved from https://doi.org/10.1007/s10596-014-9416-0 doi: 10.1007/s10596-014-9416-0

Piñero, E., Marquardt, M., Hensen, C., Haeckel, M., & Wallmann, K. (2013). Estimation of the global inventory of methane hydrates in marine sediments using transfer functions. *Biogeosciences*, *10*(2), 959–975. Retrieved from https://bg.copernicus.org/articles/10/959/2013/ doi: 10.5194/bg-10-959-2013

Portnov, A., Cook, A. E., Sawyer, D. E., Yang, C., Hillman, J. I., & Waite, W. F. (2019). Clustered bsrs: Evidence for gas hydrate-bearing turbidite complexes in folded regions, example from the perdido fold belt, northern gulf of mexico. *Earth and Planetary Science Letters*, *528*, 115843. Retrieved from https://www.sciencedirect.com/science/article/pii/S0012821X19305357 doi: https://doi.org/10.1016/j.epsl.2019.115843

Riboulot, V. (2018, 04). Geomorphology of gas hydrate-bearing pockmark. In (p. 37-48). doi: 10.1002/9781119451174.ch4

Schmidt, C., Gupta, S., Rüpke, L., Burwicz-Galerne, E., & Hartz, E. H. (2022).

Sedimentation-driven cyclic rebuilding of gas hydrates. *Marine and Petroleum Geology*, *140*, 105628. Retrieved from https://www.sciencedirect.com/science/article/pii/S0264817222001064 doi: https://doi.org/10.1016/j.marpetgeo.2022.105628

Serié, C., Huuse, M., & Schødt, N. H. (2012, 03). Gas hydrate pingoes: Deep seafloor evidence of focused fluid flow on continental margins. *Geology*, *40*(3), 207-210. Retrieved from https://doi.org/10.1130/G32690.1 doi: 10.1130/G32690.1

Waage, M., Portnov, A., Serov, P., Bünz, S., Waghorn, K. A., Vadakkepuliyambatta, S., ... Andreassen, K. (2019). Geological controls on fluid flow and gas hydrate pingo development on the barents sea margin. *Geochemistry, Geophysics, Geosystems*, *20*(2), 630-650. Retrieved from https://agupubs.onlinelibrary.wiley.com/doi/abs/10.1029/2018GC007930 doi: https://doi.org/10.1029/2018GC007930

Wohlmuth, B. (2011). Variationally consistent discretization schemes and numerical algorithms for contact problems. *Acta Numerica*, *20*, 569-734. doi: 10.1017/S0962492911000079

Wu, Y.-S., & Forsyth, P. A. (2001). On the selection of primary variables in numerical formulation for modeling multiphase flow in porous media. *Journal of Contaminant Hydrology*, *48*(3), 277-304. Retrieved from https://www.sciencedirect.com/science/article/pii/S0169772200001807 doi: https://doi.org/10.1016/S0169-7722(00)00180-7

Wuebbles, D. J., Fahey, D. W., Hibbard, K. A., DeAngelo, B., Doherty, S., Hayhoe, K., ... Weaver, C. P. (2017). Executive summary. In D. J. Wuebbles, D. W. Fahey, K. A. Hibbard, D. J. Dokken, B. C. Stewart, & T. K. Maycock (Eds.), *Climate science special report: Fourth national climate assessment, volume i* (pp. 12–34). Washington, D.C.: U.S. Global Change Research Program. doi: 10.7930/J0DJ5CTG

Yoo, D.-G., Kang, N., Yi, B., Kim, G., Ryu, B.-J., Lee, K., ... Riedel, M. (2013, 11). Occurrence and seismic characteristics of gas hydrate in the ulleung basin, east sea. *Marine and Petroleum Geology*, *47*, 236-247. doi: 10.1016/j.marpetgeo.2013.07.001

You, K., Flemings, P., Malinverno, A., Collett, T., & Darnell, K. (2019). Mechanisms of methane hydrate formation in geological systems. *Reviews of Geophysics*, *57*(4), 1146-1196. Retrieved from https://agupubs.onlinelibrary.wiley.com/doi/abs/10.1029/2018RG000638 doi: https://doi.org/10.1029/2018RG000638

You, K., Summa, L., Flemings, P., Santra, M., & Fang, Y. (2021). Three-dimensional free gas flow focuses basin-wide microbial methane to concentrated methane hydrate reservoirs in geological system. *Journal of Geophysical Research: Solid Earth*, *126*(12), e2021JB022793. Retrieved from https://agupubs.onlinelibrary.wiley.com/doi/abs/10.1029/2021JB022793 (e2021JB022793 2021JB022793) doi: https://doi.org/10.1029/2021JB022793

Yu, M., Li, W., Yang, M., Jiang, L., & Song, Y. (2017). Numerical studies of methane gas production from hydrate decomposition by depressurization in porous media. *Energy Procedia*, *105*, 250-255. Retrieved from https://www.sciencedirect.com/science/article/pii/S1876610217303442 (8th International Conference on Applied Energy, ICAE2016, 8-11 October 2016, Beijing, China) doi: https://doi.org/10.1016/j.egypro.2017.03.310

Zander, T., Haeckel, M., Berndt, C., Chi, W.-C., Klaucke, I., Bialas, J., ... n, O. A. (2017). On the origin of multiple bsrs in the danube deep-sea fan, black sea. *Earth and Planetary Science Letters*, *462*, 15-25. Retrieved from https://www.sciencedirect.com/science/article/pii/S0012821X17300122 doi: https://doi.org/10.1016/j.epsl.2017.01.006

Appendices

A Discontinuous Galerkin Method

In this section we present a discontinuous finite element method for Problem 1. In the following, all functions and parameters are assumed to be non-dimensional. The domain, $\Omega \subset \mathbb{R}^d$, will be partitioned into quadrilateral elements $\Omega_l \in \mathcal{T}_h$ where $\mathcal{T}_h$ is a mesh of the domain and $l = 1, ..., |\mathcal{T}_h|$. Broken Sobolev spaces and Bochner spaces can therefore be written as

$$\begin{aligned}
\mathcal{H}^1(\Omega, \mathcal{T}_h) &= \left\{ v \in L^2(\Omega) \;\middle|\; v|_{\Omega_l} \in \mathcal{H}^1(\Omega_l),\ \forall \Omega_l \in \mathcal{T}_h \right\}, \\
\mathcal{H}^1_b(\Omega, \mathcal{T}_h) &= \left\{ v \in \mathcal{H}^1(\Omega, \mathcal{T}_h) \;\middle|\; 0 \leq v \leq 1 \ \ a.e. \text{ in } \Omega \right\}, \\
\mathcal{C}(\mathbb{T}; \mathcal{H}^1(\Omega, \mathcal{T}_h)) &= \left\{ v : \mathbb{T} \longrightarrow \mathcal{H}^1(\Omega, \mathcal{T}_h) \;\middle|\; v \text{ is continuous} \right\}.
\end{aligned} \tag{A1}$$

F is called an interior interface if $|F| \neq 0$ and there exist Ω_F^- and Ω_F^+ in $\mathcal{T}_h$ such that $F \subseteq \Omega_F^- \cap \Omega_F^+$. $\mathbf{n}_F$ is the unit normal vector to the interface F and the direction is arbitrary but

fix. Let $\mathcal{F}^I$ be the set of all interior interfaces. Similarly, let $\mathcal{F}^B = \mathcal{F}^D \cup \mathcal{F}^N$ be the set of all the boundary faces including Dirichlet $\mathcal{F}^D$ and Neumann $\mathcal{F}^N$ boundary faces. Let $F \in \mathcal{F}^I$ and $F \subseteq \Omega_F^- \cap \Omega_F^+$ then $\forall v \in \mathcal{H}^1(\Omega, \mathcal{T}_h)$, we introduce

$$\begin{aligned} v_{_F}^- &= v|_{\Omega_{_F}^-}, & v_{_F}^+ &= v|_{\Omega_{_F}^+} \\ \{v\}_{_F} &= \frac{1}{2}(v_{_F}^- + v_{_F}^+), & [v]_{_F} &= v_{_F}^- - v_{_F}^+ \end{aligned} \tag{A2}$$

Moreover, the definitions for all boundary faces has to be adopted in a proper way. In the following, we consider flux continuity on the interfaces, i.e.,

$$[\nabla v]_{_F}.\mathbf{n}_F = 0, \tag{A3}$$

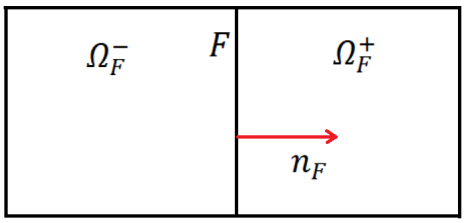

Figure A1: Two neighboring cells with F as common interface

therefore, $\forall F \in \mathcal{F}^I$ and $\forall u,\, v \in \mathcal{H}^1(\Omega, \mathcal{T}_h)$, we have

$$\mathbf{n}_F.\nabla u_{_F}^-\, v_{_F}^- - \mathbf{n}_F.\nabla u_{_F}^+\, v_{_F}^+ = \mathbf{n}_F.\{\nabla u\}_{_F}\,[v]_{_F} + \mathbf{n}_F.[\nabla u]_{_F}\,\{v\}_{_F} = \mathbf{n}_F.\{\nabla u\}_{_F}\,[v]_{_F}. \tag{A4}$$

Let $\mathcal{V} = \mathcal{C}(\mathbb{T}; \mathcal{H}^1(\Omega, \mathcal{T}_h))$ be the Bochner space for p_w, T and $\mathcal{V}_b = \mathcal{C}(\mathbb{T}; \mathcal{H}_b^1(\Omega, \mathcal{T}_h))$ be the Bochner space for $s_g, s_h, \chi_w^M, \chi_g^H, \chi_w^c$, then $\forall i \in C$, we consider the following functionals to define variational formulation for Problem 1,

$$\begin{aligned} b^i &: \mathcal{V}^2 \times \mathcal{V}_b^5 \times \mathcal{H}^1(\Omega, \mathcal{T}_h) \longrightarrow \mathbb{R}\ , \\ a^i &: \mathcal{V}^2 \times \mathcal{V}_b^5 \times \mathcal{H}^1(\Omega, \mathcal{T}_h) \longrightarrow \mathbb{R}\ , \\ a^{\sigma,i} &: \mathcal{V}^2 \times \mathcal{V}_b^5 \times \mathcal{H}^1(\Omega, \mathcal{T}_h) \longrightarrow \mathbb{R}\ , \\ l^i &: \mathcal{V}^2 \times \mathcal{V}_b^5 \times \mathcal{H}^1(\Omega, \mathcal{T}_h) \longrightarrow \mathbb{R}\ , \end{aligned} \tag{A5}$$

Thus, variational formulation for Problem 1 can be written as follows

Problem 2. *(Variational Formula) Find* $\mathbf{U} \in \mathcal{V}^2 \times \mathcal{V}_b^5$ *such that* $\forall v \in \mathcal{H}^1(\Omega, \mathcal{T}_h)$ *and* $\forall i \in C$

$$\partial_t b^i(\mathbf{U}; v) + a^i(\mathbf{U}; v) + a^{\sigma,i}(\mathbf{U}; v) = l^i(\mathbf{U}; v) + a_D^{\sigma,i}(\mathbf{U}; v) \tag{A6}$$

hold, where for $\kappa = M,\, H,\, c$

$$
\begin{aligned}
b^M(\mathbf{U};v) &:= \sum_{\Omega_l}\Big(\phi\rho_w\,\chi_w^M s_w + \phi\rho_g\,\chi_g^M s_g, v\Big)_{\Omega_l}\,,\\
a^M(\mathbf{U};v) &:= -\sum_{\Omega_l}\Big(\rho_w\chi_w^M\,\mathbf{v}_w + \rho_g\,\chi_g^M\,\mathbf{v}_g, \nabla v\Big)_{\Omega_l}\\
&\quad -\sum_{\Omega_l}\Big(\phi\,s_w\,\mathbf{J}_w^M + \rho_g\,s_g\,\mathbf{J}_g^M, \nabla v\Big)_{\Omega_l}\\
&\quad +\sum_{F\in\mathcal{F}^{I\cup D}}\Big(\Big\{\rho_w\,\chi_w^M\,\mathbf{v}_w + \rho_g\,\chi_g^M\,\mathbf{v}_g\Big\}.\boldsymbol{n}\,,\,[v]\Big)_F\\
&\qquad -\Theta\Big(\Big\{\rho_w\,\chi_w^M\,K\,\frac{k_{rw}}{\mu_w}\nabla v\Big\}.\boldsymbol{n}\,,\,[p_w]\Big)_F\\
&\quad +\sum_{F\in\mathcal{F}^{I\cup D}}\Big(\Big\{\phi\,s_w\,\mathbf{J}_w^M + \phi\,s_g\,\mathbf{J}_g^M\Big\}.\boldsymbol{n}\,,\,[v]\Big)_F\\
&\quad +\sum_{F\in\mathcal{F}^{N}}\Big((\rho_w\,\chi_w^M\,\mathbf{v}_w + \phi\,s_w\,\mathbf{J}_w^M + \rho_g\,\chi_g^M\,\mathbf{v}_g + \phi\,s_g\,\mathbf{J}_g^M).\boldsymbol{n}\,,\,v\Big)_F\,,\\
a^{\sigma,M}(\mathbf{U};v) &:= \sum_{F\in\mathcal{F}^{I\cup D}}\Big(\sigma_p\,[p_w],[v]\Big)_F\,,\quad a_D^{\sigma,M}(\mathbf{U};v) := \sum_{F\in\mathcal{F}^{D}}\Big(\sigma_p\,p_w^D, v\Big)_F\,,\\
l^M(\mathbf{U};v) &:= \sum_{\Omega_l}(\dot{g}^M, v)_{\Omega_l}\,,
\end{aligned}
\tag{A7}
$$

$$
\begin{aligned}
b^h(\mathbf{U};v) &:= \sum_{\Omega_l}\Big(\phi\,\rho_h\,s_h, v\Big)_{\Omega_l}\,,\\
a^h(\mathbf{U};v) &:= 0\,,\\
a^{\sigma,h}(\mathbf{U};v) &:= \sum_{F\in\mathcal{F}^{I}}\Big(\sigma_s\,[s_h],[v]\Big)_F\,,\quad a_D^{\sigma,h}(\mathbf{U};v) := 0,\\
l^h(\mathbf{U};v) &:= \sum_{\Omega_l}(\dot{g}_h, v)_{\Omega_l}\,,
\end{aligned}
\tag{A8}
$$

$$
\begin{aligned}
b^H(\mathbf{U};v) &:= \sum_{\Omega_l}\Big(\phi\rho_w\,\chi_w^H s_w + \phi\rho_g\,\chi_g^H s_g, v\Big)_{\Omega_l}\,,\\
a^H(\mathbf{U};v) &:= -\sum_{\Omega_l}\Big(\rho_w\chi_w^H\,\mathbf{v}_w + \rho_g\,\chi_g^H\,\mathbf{v}_g, \nabla v\Big)_{\Omega_l}\\
&\quad -\sum_{\Omega_l}\Big(\phi\,s_w\,\mathbf{J}_w^H + \rho_g\,s_g\,\mathbf{J}_g^H, \nabla v\Big)_{\Omega_l}\\
&\quad +\sum_{F\in\mathcal{F}^{I\cup D}}\Big(\Big\{\rho_w\,\chi_w^H\,\mathbf{v}_w + \rho_g\,\chi_g^H\,\mathbf{v}_g\Big\}.\boldsymbol{n}\,,\,[v]\Big)_F\\
&\quad\quad -\Theta\Big(\Big\{\rho_g\,\chi_g^H\,K\,\frac{k_{rg}}{\mu_g}\nabla v\Big\}.\boldsymbol{n}\,,\,[s_g]\Big)_F\\
&\quad +\sum_{F\in\mathcal{F}^{I\cup D}}\Big(\Big\{\phi\,s_w\,\mathbf{J}_w^H + \phi\,s_g\,\mathbf{J}_g^H\Big\}.\boldsymbol{n}\,,\,[v]\Big)_F\\
&\quad +\sum_{F\in\mathcal{F}^{N}}\Big((\rho_w\,\chi_w^H\,\mathbf{v}_w + \phi\,s_w\,\mathbf{J}_w^H + \rho_g\,\chi_g^H\,\mathbf{v}_g + \phi\,s_g\,\mathbf{J}_g^H).\boldsymbol{n}\,,\,v\Big)_F\,,\\
a^{\sigma,H}(\mathbf{U};v) &:= \sum_{F\in\mathcal{F}^{I\cup D}}\Big(\sigma_s\,[s_g],[v]\Big)_F\,,\;\; a_D^{\sigma,H}(\mathbf{U};v) := \sum_{F\in\mathcal{F}^{D}}\Big(\sigma_s\,s_g^D, v\Big)_F\,,\\
l^H(\mathbf{U};v) &:= \sum_{\Omega_l}(\dot{g}^H, v)_{\Omega_l}\,,
\end{aligned}
\tag{A9}
$$

$$
\begin{aligned}
b^e(\mathbf{U};v) &:= \sum_{\Omega_l}\Big((1-\phi)\,\rho_s\,u_s\; + \phi\,(\rho_w\,u_w\,s_w + \rho_g\,u_g\,s_g + \rho_h\,u_h\,s_h), v\Big)_{\Omega_l}\,,\\
a^e(\mathbf{U};v) &:= -\sum_{\Omega_l}\Big(\rho_w\,h_w\,\mathbf{v}_w + \rho_g\;h_g\,\mathbf{v}_g - k_{eff}^{th}\nabla T, \nabla v\Big)_{\Omega_l}\\
&\quad +\sum_{F\in\mathcal{F}^{I\cup D}}\Big(\Big\{\rho_w\,h_w\,\mathbf{v}_w + \rho_g\;h_g\,\mathbf{v}_g - k_{eff}^{th}\nabla T\Big\}.\boldsymbol{n}\,,\,[v]\Big)_F\\
&\quad\quad +\Theta\Big(\Big\{-k_{eff}^{th}\nabla v\Big\}.\boldsymbol{n}\,,\,[T]\Big)_F\\
&\quad +\sum_{F\in\mathcal{F}^{N}}\Big((\rho_w\,h_w\,\mathbf{v}_w + \rho_g\,h_g\,\mathbf{v}_g - k_{eff}^{th}\nabla T).\boldsymbol{n}\,,\,v\Big)_F.\\
a^{\sigma,e}(\mathbf{U};v) &:= \sum_{F\in\mathcal{F}^{I\cup D}}\Big(\sigma_T\,[T],[v]\Big)_F\,,\;\; a_D^{\sigma,e}(\mathbf{U};v) := \sum_{F\in\mathcal{F}^{D}}\Big(\sigma_T\,T^D, v\Big)_F\,,\\
l^e(\mathbf{U};v) &:= \sum_{\Omega_l}(\dot{Q}_h, v)_{\Omega_l}\,,
\end{aligned}
\tag{A10}
$$

$$
\begin{aligned}
b^{ncp1}(\mathbf{U};v) &:= 0,\\
a^{ncp1}(\mathbf{U};v) &:= \sum_{\Omega_l}\Big(s_g - max\{0,\,s_g - 1 + \chi_g^M + \chi_g^H\}\,,\,v\Big)_{\Omega_l}\,,\\
a^{\sigma,ncp1}(\mathbf{U};v) &:= \sum_{F\in\mathcal{F}^{I}}\Big(\sigma_x\,[\chi_g^H],[v]\Big)_F\,,\;\; a_D^{\sigma,ncp1}(\mathbf{U};v) := 0,\\
l^{ncp1}(\mathbf{U};v) &:= 0\,,
\end{aligned}
\tag{A11}
$$

$$
\begin{aligned}
b^{ncp2}(\mathbf{U};v) &:= 0,\\
a^{ncp2}(\mathbf{U};v) &:= \sum_{\Omega_l}\Big(s_w - max\{0,\, s_w - 1 + \chi_w^M + \chi_w^H + \chi_w^c\}\,,\, v\Big)_{\Omega_l}\,,\\
a^{\sigma,ncp2}(\mathbf{U};v) &:= \sum_{F\in\mathcal{F}^I}\Big(\sigma_x\,[\chi_w^M],[v]\Big)_F\,, a_D^{\sigma,ncp2}(\mathbf{U};v) := 0,\\
l^{ncp2}(\mathbf{U};v) &:= 0\,,
\end{aligned}
\tag{A12}
$$

$$
\begin{aligned}
b^{c}(\mathbf{U};v) &:= \sum_{\Omega_l}\Big(\phi\rho_w\,\chi_w^c s_w, v\Big)_{\Omega_l}\,,\\
a^{c}(\mathbf{U};v) &:= -\sum_{\Omega_l}\Big(\rho_w\chi_w^c\,\mathbf{v}_w + \phi\,s_w\,\mathbf{J}_w^c, \nabla v\Big)_{\Omega_l}\\
&\quad + \sum_{F\in\mathcal{F}^{I\cup D}}\Big(\Big\{\rho_w\,\chi_w^c\,\mathbf{v}_w + \phi\,s_w\,\mathbf{J}_w^c\Big\}.\boldsymbol{n}\,,\,[v]\Big)_F\\
&\quad\quad - \Theta\Big(\Big\{\phi\,s_w\,\tau\mathbf{D}_w^c\rho_w\nabla v\Big\}.\boldsymbol{n}\,,\,[\chi_w^c]\Big)_F\\
&\quad + \sum_{F\in\mathcal{F}^N}\Big((\rho_w\,\chi_w^c\,\mathbf{v}_w + \phi\,s_w\,\mathbf{J}_w^\kappa).\boldsymbol{n}\,,\,v\Big)_F\,,\\
a^{\sigma,c}(\mathbf{U};v) &:= \sum_{F\in\mathcal{F}^{I\cup D}}\Big(\sigma_x\,[\chi_w^c],[v]\Big)_F\,,\;\; a_D^{\sigma,c}(\mathbf{U};v) := \sum_{F\in\mathcal{F}^D}\Big(\sigma_x\,\chi_w^{c,D}, v\Big)_F\,,\\
l^{c}(\mathbf{U};v) &:= \sum_{\Omega_l}(\dot{g}^c, v)_{\Omega_l}\,,
\end{aligned}
\tag{A13}
$$

and $\sigma_s,\ \sigma_p,\ \sigma_x,\ \sigma_T$ are the positive penalty coefficients corresponding to the saturation, pressure, mole fraction and temperature functions respectively, $\Theta = 1, -1, 0$ in the cases of symmetric, nonsymmetric and incomplete forms of variational formulation for Problem 1.

We introduce the following vector notations:

$$
\begin{aligned}
b(\mathbf{U};v) &= \big[b^i(\mathbf{U};v)\big]_{i\in C}\,, \qquad a(\mathbf{U};v) = \big[a^i(\mathbf{U};v)\big]_{i\in C}\,,\\
l(\mathbf{U};v) &= \big[l^i(\mathbf{U};v)\big]_{i\in C}\,, \qquad a^\sigma(\mathbf{U};v) = \big[a^{\sigma,i}(\mathbf{U};v)\big]_{i\in C}\,,\;\; a_D^\sigma(\mathbf{U};v) = \big[a_D^{\sigma,i}(\mathbf{U};v)\big]_{i\in C}
\end{aligned}
\tag{A14}
$$

Let $q_i \geq 0$ be an integer for every $i \in C$. We consider the finite-dimensional subspace of broken Sobolev spaces (A1)

$$
\begin{aligned}
\mathcal{S}_h^{q_i} &= \Big\{v\in L^2(\Omega)\;\Big|\;\; v|_{_{\Omega_l}}\in\mathbb{P}^{q_i},\ \forall\Omega_l\in\mathcal{T}_h\Big\}, \quad \mathcal{S}_h^{q_i}\subset\mathcal{H}^k(\Omega,\mathcal{T}_h),\;\; k\geq 1\\
\mathcal{K}_h^{q_i} &= \Big\{v\in\mathcal{S}_h^{q_i}\;\Big|\; 0\leq v\leq 1,\ a.e.\text{ in }\ \Omega\Big\}, \qquad\qquad \mathcal{K}_h^{q_i}\subset\mathcal{H}_b^k(\Omega,\mathcal{T}_h),\;\; k\geq 1.
\end{aligned}
\tag{A15}
$$

Let $\{\phi_{l,j},\ l=1,...,|\mathcal{T}_h|,\ j=1,...,d(q_i)\}$ be the basis of $\mathcal{S}_h^{q_i}$, such that

$$\begin{aligned} \mathcal{S}_h^{q_i} &= \text{span}\{\phi_{l,j}\}\ , \qquad \phi_{l,j} : \Omega_l \longrightarrow \mathbb{R}, \\ \forall v \in \mathcal{S}_h^{q_i}\ , &\qquad v|_{\Omega_l} = \sum_{j=1}^{d(q_i)} v_{l,j}(t)\phi_{l,j}(x), \end{aligned} \tag{A16}$$

where $d(q_i)$ is the number of basis functions defined on one element of triangulation ($\Omega_l \in \mathcal{T}_h$), for example, if $q_i = 1$ and Ω_l is a quadrilateral, then $d(1) = 2,\ 4$ in 1D and 2D domain. After extending the basis functions to the domain, Ω, $\forall k = (l-1)d(q_i)+j$, we write:

$$\begin{aligned} \varphi_k : \Omega \longrightarrow \mathbb{R}, &\qquad \varphi_k(x) = \begin{cases} \phi_{l,j}(x) & x \in \Omega_l \\ 0 & x \notin \Omega_l \end{cases} \\ \forall v \in \mathcal{S}_h^{q_i}\ , &\qquad v = \sum_{k=1}^{\mathtt{N}_h^{q_i}} v_k(t)\varphi_k(x), \\ \mathcal{S}_h^{q_i} = \text{span}\ \mathcal{S}_b^i, &\qquad \mathcal{S}_b^i = \{\varphi_k^i,\ j=1,...,\mathtt{N}_h^{q_i}\} \end{aligned} \tag{A17}$$

where $\mathtt{N}_h^{q_i} = |\mathcal{T}_h|d(q_i)$. The primary variables can be written in terms of the basis functions as follows:

$$\mathbf{U}_i(x,t) = \sum_k \mathbf{U}_{i,k}(t)\varphi_k^i(x)\ , \qquad i \in C \tag{A18}$$

Let $\mathcal{V}_h^i = \mathcal{C}(\mathbb{T}; \mathcal{S}_h^{q_i})$ be the finite dimensional Bochner subspace for $i \in \{p_w,\ T\}$ and $\mathcal{V}_{h,b}^i = \mathcal{C}(\mathbb{T}; \mathcal{K}_h^{q_i})$ be the finite dimensional Bochner subspace for $i \in \{s_g, s_h, \chi_w^M, \chi_g^H, \chi_w^c\}$. Now interior and boundary penalty discontinuous Galerkin (IPDG) method for the system (15) can be written as follows

Problem 3. *(DG formula) Find* $\mathbf{U} \in \mathcal{V}_h^M \times \mathcal{V}_h^e \times \mathcal{V}_{b,h}^H \times \mathcal{V}_{b,h}^h \times \mathcal{V}_{b,h}^{ncp1} \times \mathcal{V}_{b,h}^{ncp2} \times \mathcal{V}_{b,h}^c$ *such that* $\forall \psi_j^i \in \mathcal{S}_b^i$ *and* $\forall i \in C$

$$\partial_t b^i(\mathbf{U};\psi_j^i) + a^i(\mathbf{U};\psi_j^i) + a^{\sigma,i}(\mathbf{U};\psi_j^i) = l^i(\mathbf{U};\psi_j^i) + a_D^{\sigma,i}(\mathbf{U};\psi_j^i) \tag{A19}$$

hold.

A1 Implicit Euler Method

In this section, we apply Implicit Euler method for the system (A19). To do so, we consider a partition $t_0 := 0 < t_1 < ... < t_m := t_{end}$ of the time interval $\mathbb{T}$. By defining $\Delta t_n := t_{n+1} - t_n$, We use finite difference approximation of the time derivative,

$$\partial_t b(\mathbf{U};\psi) \approx \Delta t_n^{-1}\Big(b_h(\mathbf{U}^{n+1};\psi) - b_h(\mathbf{U}^n;\psi)\Big) \tag{A20}$$

where $\mathbf{U}^n := \mathbf{U}(t_n)$. Let $\mathbb{U}$ be the coefficient vector of the primary variables $\mathbf{U}$ w.r.t basis functions in $\mathcal{S}_b^i$, i.e., $\mathbb{U}$ is a row vector with $\mathbf{N}_h = \sum_{i \in C} \mathtt{N}_h^{q_i}$ elements.

Using finite difference approximation of the time derivative (A20), we introduce the residual functional $\mathcal{R}_j^i(\mathbb{U}^{n+1}, \mathbf{U}^n)$ for every $\psi_j^i \in \mathcal{S}_b^i,\ j = 1, ..., \mathtt{N}_h^{q_i}$ and $\forall i \in C$ as follows:

$$\begin{aligned}\mathcal{R}_j^i(\mathbb{U}^{n+1}, \mathbf{U}^n) :=& \Delta t_n^{-1}\Big(b^i(\mathbf{U}^n; \psi_j^i) - b^i(\mathbf{U}^{n+1}; \psi_j^i)\Big) + l^i(\mathbf{U}^{n+1}; \psi_j^i) \\ &- a^i(\mathbf{U}^{n+1}; \psi_j^i) - a^{\sigma,i}(\mathbf{U}^{n+1}; \psi_j^i) + a_D^{\sigma,i}(\mathbf{U}^{n+1}; \psi_j^i) = 0,\end{aligned} \tag{A21}$$

The nonlinear residual equations can then be written in compact form as follows:

$$\mathcal{R}(\mathbb{U}^{n+1}, \mathbf{U}^n) = \big[\mathcal{R}_j^i(\mathbb{U}^{n+1}, \mathbf{U}^n)\big]_{i,j} = 0, \quad i \in C,\ j = 1, ..., \mathtt{N}_h^q, \quad \mathcal{R}(\mathbb{U}^{n+1}, \mathbf{U}^n) \in \mathbb{R}^{\mathbf{N}_h}. \tag{A22}$$